Applied Catalysis B: Environmental 199 (2016) 260–271

Contents lists available at ScienceDirect

Applied Catalysis B: Environmental

journal homepage: www.elsevier.com/locate/apcatb

Harnessing self-supported Au nanoparticles on layered double hydroxides comprising Zn and Al for enhanced phenol decomposition under solar light

Gaku Mikami [a], Florentina Grosu [b], Shogo Kawamura [a], Yusuke Yoshida [a], Gabriela Carja [b,*], Yasuo Izumi [a,*]

[a] Department of Chemistry, Graduate School of Science, Chiba University, Yayoi 1-33, Inage-ku, Chiba 263-8522, Japan
[b] Department of Chemical Engineering, Faculty of Chemical Engineering and Environmental Protection, Technical University "Gh. Asachi" of Iasi, Bd. Mangeron No. 71, Iasi 700554, Romania

ARTICLE INFO

Article history:
Received 6 April 2016
Received in revised form 8 June 2016
Accepted 9 June 2016
Available online 17 June 2016

Keywords:
Layered double hydroxide
Gold nanoparticles
Electron transfer
Phenol
Photo-decomposition

ABSTRACT

Gold nanoparticles (AuNPs) self-coupled on semiconductors have attracted extensive attentions in the field of catalysis, however, the progress in understanding and optimizing their photocatalytic performance in response to solar light irradiation is limited. In this paper, a series of AuNPs with Zn_2Al-layered double hydroxide (LDH) as support was fabricated via self-assembly routes at room temperature and the tuned oxidation state of AuNPs (as Au^0, Au^{3+} as well as mixed Au^0/Au^{3+}) was revealed to have a crucial effect on establishing their photocatalytic efficiency for the degradation of phenol from aqueous solution under solar irradiation. X-ray absorption near-edge structure (XANES) and extended X-ray absorption fine structure (EXAFS) analyses permitted to characterize the specific interactions of Zn_2Al-LDH with AuNPs and to verify that the state of Au^0/Au^{3+}NPs appears due to the electron transfer from Zn_2Al-LDH to AuNPs when Zn_2Al-LDH reconstruction in the aqueous solution of $Au(O_2CCH_3)_3$ was achieved under solar irradiation. On the basis of these AuNPs–Zn_2Al-LDH systems, the possible roles of Au^0, Au^{3+} or Au^0/Au^{3+} in establishing synergetic effects with Zn_2Al-LDHs supports for enhancing the photocatalytic response induced by the irradiation with solar light, for manipulating the mechanism, and the catalyst stability in phenol degradation process, are critically discussed.

1. Introduction

Gold nanoparticles (AuNPs) have received increasing attentions in catalysis since Hutchings et al. [1] and Haruta et al. [2] demonstrated excellent performances of gold-based catalysts in low-temperature oxidation of CO [3]. AuNPs supported on solids with high surface area are used for a large variety of catalytic reactions, e.g. photocatalysis, cross coupling, sequential oxidative addition, benzylation of aromatics, oxidative C—C coupling, amination, and nucleophilic addition [4–8]. The support materials play not only the role of stabilizing AuNPs at different oxidation state ($Au^{\delta+}$, Au^+, or Au^{3+}) or controlling their dispersion level (nanoparticle size) but also might act as a buffer for the electron transfer to AuNPs, and thus to reduce the charge-carrier recombination during the photo-responsive processes [9–11]. Furthermore, (1) the particle size-dependent photoresponsive characteristics of AuNPs, e.g. surface plasmon resonance (SPR) response, (2) the photo-functionality of the support, and (3) the charge–transfer characteristics from AuNPs to support materials are the recent key issues in designing efficient nano-gold composites as solar-responsive photocatalysts [12–14].

Among the numerous materials of large surface area, layered double hydroxides (LDHs) exhibits unique features not found in other solid supports if used as support materials for AuNPs, thus making AuNPs/LDHs composites specific catalysts [15]. The flexibility of the LDHs composition, their semiconducting characteristics [4], and their high adsorption capacity enables to tune the electronic density at the interface between AuNPs and LDHs. Furthermore, LDHs own a unique self-repairing property to reconstruct its layered structure, after being transformed through calcination into mixtures of metal oxides by the calcination, utilizing its structural "memory effect" to restore original layered structure from mixed oxides. Utilizing the structural memory effect of LDHs, we recently reported a simple, one-step route to fabricate

* Corresponding authors.
E-mail addresses: carja@uaic.ro (G. Carja), yizumi@faculty.chiba-u.jp (Y. Izumi).

http://dx.doi.org/10.1016/j.apcatb.2016.06.031
0926-3373/

AuNPs directly on Zn–Al–Ce LDHs [16] and Zn–Ga LDHs [17]. This method used the capability of LDH matrix to form self-supported AuNPs on LDHs, by exploiting the property of LDHs to restore its original layered structure in the aqueous solutions of gold salts, e.g. $AuCl_3$ and $Au(CH_3COO)_3$, without using any organic additives as surfactant and/or stabilizer for AuNPs.

In a related precedent work, it was revealed that the microscopic morphology of LDHs has an important effect on the location and the size of AuNPs [6]. Recently, Liu and co-workers [7] demonstrated that the synergy between AuNPs and LDHs in AuNPs–Cr-LDHs composites increased if the Cr content was increased in the Cr-LDHs as a support. To date, despite the significant interests in catalysis using the AuNPs composites, maximizing their efficiency under irradiation with solar light still remains a meaningful challenge and the examples in scientific literature are few [18,19]. It was demonstrated that the specific charge transfer between AuNPs and a semiconductor support was able to reduce the charge recombination rates and to increase the photocatalytic efficiency [20]. Hence, to design AuNPs–LDHs composites as active photocatalysts under solar irradiation, one of the keys is to establish favourable charge-transfer pathway between the supported AuNPs and LDHs.

Herein, we investigate facile self-assembly routes at room temperature to obtain novel AuNPs–Zn_2Al-LDH photocatalysts with tuned oxidation state of AuNPs, as Au^0, Au^{3+} as well as a mixture of Au^0/Au^{3+}. Furthermore, X-ray absorption near-edge structure (XANES) and extended X-ray absorption fine structure (EXAFS) analyses permits to demonstrate that the mixed state of Au^0/Au^{3+} is the result of an electron transfer from Zn_2Al-LDH to AuNPs when Zn_2Al-LDH reconstruction in the aqueous solution of gold acetate was achieved under solar irradiation. To benchmark the suitability of AuNP–Zn_2Al-LDH for solar photocatalysis, they were tested for the phenol photo-decomposition. This reaction is not only a quite well-understood model reaction, but also satisfies an empirical requirement to eliminate a common pollutant, phenol, in the wastewater streams worldwide. We provide compelling evidence that AuNPs are the catalytically active sites for photodegrading phenol under irradiation with simulated solar light although the transfer interactions between AuNPs and Zn_2Al-LDH were crucial to enhance the photocatalytic efficiency.

2. Experimental

2.1. Synthesis of LDH

An aqueous solution of Zn nitrate hexahydrate (>99%, Wako Pure Chemical) and Al nitrate nonahydrate (>99.9%, Wako Pure Chemical) with the Zn/Al atomic ratio of 2.0 in deionized water (<0.06 $\mu S\,cm^{-1}$) with the concentration of $[Zn^{2+}]+[Al^{3+}]=1.2$ M, an aqueous solution of NaOH (1.92 M; >97%, Kanto Chemical), and Na_2CO_3 (0.8 M; >99.8%, Wako Pure Chemical) in deionized water were simultaneously added to a flask using a magnetic stirrer at a speed of 900 rates per minute (rpm) for 48 h. The precipitate was filtered and washed with deionized water and dried at 333 K for 24 h [21–23]. The resultant sample was denoted as Zn_2Al-LDH (Table 1a).

2.2. AuNPs on Zn_2Al-LDH by the reconstruction method

AuNPs supported on Zn_2Al-LDH was obtained exploring the structural reconstruction of LDH in the aqueous solutions containing Au^{3+} ions [21]. Namely, 1.20 g Zn_2Al-LDH powder was calcined in an oven at 773 K for 8 h. The resulted calcined powder was cooled down in the oven till 473 K and slowly added into 250 mL aqueous solution of Au(III) acetate (0.10 g or 0.30 g; >99.9%, Alfa Aesar) with a stirring at a rate of 900 rpm. The reaction mixture

Table 1
Characteristics of Au/Zn_2Al-LDH samples.

Entry	Sample name	Au						S_{BET} ($m^2\,g^{-1}$)[e]	E_g (eV)	Photocatalytic rates ($\mu mol\,L^{-1}\,h^{-1}$)
		Contents (wt%)	$Au^0:Au^{3+}$	Particle size distribution (nm)	Mean size (nm)		Exposed Au^0 ($\mu mol\,g_{cat}^{-1}$)[d]			
				TEM	TEM	EXAFS				
a	Zn_2Al-LDH	–	–	–	–	–	–	97	5.7	25
b	Au/Zn_2Al-Rec-1[c]	4.8	0: 100	1.1–13.6	4.7 (±2.4)		0	81	3.1	125
c	Au/Zn_2Al-Rec-2	16	0: 100	1.8–18.0	4.9 (±2.1)		0	59	2.5	47
d	Au/Zn_2Al-Rec-3-Light[a,c]	4.8	65: 35	1.9–25.4	8.5 (±3.6)	2.5	27	79	2.6	199
e	Au/Zn_2Al-Imp-$NaBH_4$[c]	2.2	85: 15	2.2–7.7	4.1 (±1.0)	4.8	31	54	–[f]	42
f	Au/Zn_2Al-Imp-Lysine[c]	1.9	100: 0	3.9–14.0	7.3 (±2.0)	5.3	19	67	–[f]	43
g	Au/Zn_2Al-Light[c]	4.8						–	–[f]	68

[a]Irradiated by Solar light simulator during LDH the reconstruction for 20 min for Au/Zn_2Al-Rec-1. [b]Evaluated from XANES edge jump values. [c]For Au/Zn_2Al-Rec-1, Au/ZnAl-Rec-3, Au/ZnAl-Imp-$NaBH_4$, Au/Zn_2Al-Imp-Lysine, and Au/Zn_2Al-Light the amount of gold introduced during the sample preparation compared to the amount of support material was the same (5:100). [d]Estimated based on Au content in catalyst, Au^0:Au^{3+} ratio, mean Au size by TEM, and the correlation between dispersion and diameter of fcc cubo-octahedron particles [41]. [e]BET surface area evaluated for samples after photocatalytic phenol decomposition tests for 5 h. [f]It was difficult to determine the absorption edge due to the overlap of broad SPR peaks.

was stirred at the rate of 900 rpm and 290 K for 3 h. Then, the precipitate was centrifuged at a speed of 10 000 rpm and dried at 358 K. The sample is denoted as Au/Zn_2Al-Rec-1 (4.8 wt% of Au) and Au/Zn_2Al-Rec-2 (16 wt% of Au), respectively (Table 1b, c). Separately, after adding the calcined LDH into the Au(III) acetate (0.10 g) solution, the resulted suspension was irradiated using a Solar simulator (Model US 800, Unnasol, Germany) for 20 min, stirred at the same rate (900 rpm). The sample is denoted as Au/Zn_2Al-*Rec*-3-Light (Table 1d).

As a comparison, 0.24 g Zn_2Al-LDH powder was mixed with 250 mL aqueous solution of Au(III) acetate (0.020 g) with a stirring at a rate of 900 rpm and irradiated using a Solar simulator for 20 min. Then, the reaction mixture was stirred at a rate of 900 rpm and 290 K for 3 h. Then, the precipitate was filtered using JGWP04700 filter, washed using JGWP04700 filter with deionized water and ethanol (total 250 mL for each), and dried under vacuum at 290 K for 24 h. The sample was denoted as Au/Zn_2Al-Light (4.8 wt% Au; Table 1g).

2.3. AuNPs on Zn_2Al-LDH by impregnation of $HAuCl_4$ followed by liquid reduction

0.044 g of hydrochloroauric acid tetrahydrate (> 99.9%, Alfa Aesar) was dissolved in 10 mL of deionized water. 0.42 g of Zn_2Al-LDH was added to the aqueous solution and the mixture was stirred at a rate of 900 rpm and 290 K for 12 h. The precipitate was filtered using a membrane filter (JGWP04700 filter, Omnipore) and washed with deionized water (total 250 mL), and dried under vacuum at 290 K for 24 h. Obtained powder was added to 10 mL of dehydrated toluene (> 99.5%, Wako Pure Chemical) and 0.0126 g of $NaBH_4$ (> 95%, Wako Pure Chemical) was added to the suspension. After stirring for 10 min, 3 mL of ethanol (> 99.5%, Wako Pure Chemical) was added and the mixture was stirred at a rate of 900 rpm and 290 K for 6 h. The precipitate was filtered and washed using JGWP04700 filter with deionized water and ethanol (total 250 mL for each), and dried under vacuum at 290 K for 24 h [15]. The sample was denoted as Au/Zn_2Al-Imp-$NaBH_4$ (Table 1e).

Separately, 0.30 g of Zn_2Al-LDH was dispersed in 10 mL of deionized water. To ensure a uniform dispersion, the suspension was ultrasonicated (430 W, 38 kHz) for 10 min. Then, 0.031 g of $HAuCl_4{\cdot}4H_2O$ in aqueous solution (20 mL), 0.036 g of L-lysine (98%, Sigma–Aldrich Chemie) in aqueous solution (4.0 mL), and 0.026 g of $NaBH_4$ in aqueous solution (2.0 mL) were added sequentially to the above suspension with a dropping speed of 1.0 mL min^{-1} and stirred at a rate of 900 rpm. Afterwards, dilute hydrochloric acid (Wako Pure Chemical) was added to adjust the pH value to 9.5. The mixed solution was stirred for 1 h and left standing for 24 h. The precipitate was filtered using JGWP04700 filter and washed with deionized water and ethanol (total 250 mL for each), and dried at 333 K for 12 h [24]. The sample was denoted as Au/Zn_2Al-Imp-Lysine (Table 1f).

2.4. X-ray diffraction (XRD)

XRD pattern was observed using a D8 ADVANCE diffractometer (Bruker) at the Center for Analytical Instrumentation, Chiba University, at a Bragg angle (θ_B) of $2\theta_B = 3^\circ$–60° with a scan step of 0.01° and a scan rate of 5 s per step. The measurements were performed at 40 kV and 40 mA using Cu Kα emission and a nickel filter.

2.5. UV–visible spectroscopy

Optical spectroscopic measurements were performed using a UV–visible spectrophotometer (Model V-650, JASCO) using D_2 and halogen lamps for wavelengths between 200 and 340 nm and between 340 and 800 nm, respectively. An integrating sphere (Model ISV-469, JASCO) was used for the diffuse reflectance (DR) measurements. The samples were set in contact with the quartz window glass in a gas-tight DR cell. The measurements were performed at 290 K within the wavelength range 200–800 nm using 70 mg of sample. DR spectra were converted to absorption spectra on the basis of the Kubelka–Munk equation [22,25,26]. The band-gap value was evaluated on the basis of either simple extrapolation of the absorption edge or the fit to the equation of Davis and Mott [22,26],

$$\alpha \times h\nu \propto (h\nu - E_g)^n \quad (1)$$

in which α, h, and ν are the absorption coefficient, Planck's constant, and the frequency of light, respectively, and n is 1/2, 3/2, 2, and 3 for allowed direct, forbidden direct, allowed indirect, and forbidden indirect transitions, respectively [27].

2.6. Transmission electron microscopy (TEM)

High-resolution (HR)-TEM images were observed using a Model H-7650, Hitachi operating at 100 kV. Tungsten filament was used in the electron gun and the samples were mounted on a conducting carbon with Cu grid mesh (150 mesh per inch) and the magnification was between 60 000 and 200 000 times [28].

2.7. Au L_3-edge XANES and EXAFS

Au L_3-edge XANES and EXAFS spectra were measured at 290 K in a transmission mode on beamline NW10A in the Photon Factory Advanced Ring at the High Energy Accelerator Research Organization (Tsukuba). The storage ring energy was 6.5 GeV and the ring current was 46.6–36.1 mA. A Si (3 1 1) double-crystal monochromator and platinum-coated focusing cylindrical mirror were inserted into the X-ray beam path. The X-ray intensity was reduced at 65% of the maximum flux using a piezo translator set to the crystal to suppress the effects of higher harmonics other than 3 1 1 reflection [29]. The slit opening size was 1 mm (vertical) × 2 mm (horizontal) in front of the ionization chamber. The Au L_3-edge absorption energy was calibrated to 11 921.2 eV for the spectrum of Au metal foil [30–32].

The XANES and EXAFS data were analyzed using an XDAP package [33]. The pre-edge background was approximated by a modified Victoreen function $C_2/E^2 + C_1/E + C_0$. The background of the post-edge oscillation μx was approximated by a smoothing spline function and calculated by an equation for the number of data points, where k is the angular wavenumber of photoelectrons.

$$\sum_{i=1}^{\text{Data Points}} \frac{(\mu x_i - BG_i)^2}{exp(-0.075k_i^2)} \leq \text{smoothig factor} \quad (2)$$

Multiple-shell curve-fit analyses were performed for the Fourier-filtered k^3-weighted EXAFS data in k- and interatomic distance (R)-space using empirical amplitude extracted from the EXAFS data for Au_2O_3 powder and Au metal foil. The R value and its associated coordination number (N) for the Au–O and Au–Au pairs were set to 0.201 3 nm with the N value of 4 and 0.288 4 nm with the N value of 12, respectively [17]. The many-body reduction factor $S_0{}^2$ was assumed to be equal for both the sample and the reference.

2.8. Brunauer, Emmett, and Teller (BET) surface area measurements

N_2 adsorption isotherms were measured at 77.15 K on a Quantachrome Autosorb-1MP automated gas adsorption system. Prior to the measurements, the samples were heated for 12 h under vacuum at 383 K. The BET specific surface area (S_{BET}) was calculated

by using the standard Brunauer, Emmett, and Teller method on the basis of adsorption–desorption data [22,23].

2.9. Photocatalytic tests for phenol decomposition

Appropriate amounts of a catalyst were suspended in a phenol solution (50 mg L^{-1}) in a batch reactor using a catalyst of 0.5 g L^{-1}. The temperature was kept constant at 298 K. After 30 min in darkness to ensure the adsorption equilibrium of phenol on the catalyst, the reactor was irradiated from a solar simulator (Model US 800, Unnasol, Germany) for photocatalytic reaction tests. The sampling of the solution was carried out using a 1 mL pipet every 20 min for 7 h of irradiation. The sampled 1.0 mL of reaction suspension was centrifuged to separate solution from the photocatalyst. The solution was immediately analyzed using UV–visible spectrometer (Model V-550, JASCO) to determine the concentrations of remained phenol and transformed compounds from phenol (*p*-benzoquinone, muconic acid, catechol, and hydroquinone) [34]. The UV–visible spectra for standard aqueous solution of *p*-benzoquinone (Wako Pure Chemical, >98%), trans,trans-muconic acid (Tokyo Chemical Industry, 98%), phenol (Wako Pure Chemical, >99%), catechol (Wako Pure Chemical, >99%), and hydroquinone (Wako Pure Chemical, >99%) were also measured in transmission mode at 290 K.

The peaks in the UV–visible spectra at 197 nm, 210 nm, 248 nm, and 270 nm were assigned to π–π* and n–π* transition for aromatic ring [35], *p*-benzoquinone, and phenol [36], respectively, and the spectra were deconvoluted using the four Gaussian peaks as follows:

$$f(x) = a_1 exp\left\{-\left(\frac{x-197}{b_1}\right)^2\right\} + a_2 exp\left\{-\left(\frac{x-210}{b_2}\right)^2\right\} + a_3 exp\left\{-\left(\frac{x-248}{b_3}\right)^2\right\} + a_4 exp\left\{-\left(\frac{x-270}{b_4}\right)^2\right\} \quad (3)$$

The a_n and b_n ($n = 1, 2, 3, 4$) were the absorbance and peak width in nm, respectively. The b_1, b_2, b_3, and b_4 values resulted in within the range of 6.0–10, 11–30, 12–30, and 8.0–22 nm, respectively. To reconfirm the assignment and evaluation of reactants and intermediate compounds, especially phenol and *p*-benzoquinone, the reaction solution was also analyzed high-pressure liquid chromatograph (HPLC; Model Prominence-i, Shimadzu) [37].

3. Results

3.1. XRD

The XRD patterns of Zn_2Al-LDH, Au/Zn_2Al-Rec-1, Au/Zn_2Al-Rec-2, Au/Zn_2Al-*Rec*-3-Light, Au/Zn_2Al-Imp-$NaBH_4$, and Au/Zn_2Al-Imp-Lysine samples are depicted in Fig. 1. The diffraction peaks common at $2\theta_B$ = 11.8°, 23.6°, 34.1°, 34.8°, 37.5°, 39.4°, 44.2°, 47.0°, 53.2°, and 56.6° were assigned to 0 0 3, 0 0 6, 1 0 1, 0 0 9, 1 0 4, 0 1 5, 1 0 7, 0 1 8, 1 0 0, and $\frac{1}{2}$ 1 1 (=0 1 $\bar{1}$ 1) diffractions for the regular layered structure of LDHs. For Au/Zn_2Al-Rec-1 and Au/Zn_2Al-*Rec*-3-Light samples, weak peaks derived from 1 0 0 and 1 0 1 reflections for wurtzite crystal of ZnO also appeared at $2\theta_B$ = 31.9° and 36.4° (marked with * in Fig. 1), respectively, suggesting the layered structure of LDH was not fully recovered. For Au/Zn_2Al-Rec-2 and Au/Zn_2Al-*Rec*-3-Light, a weak peak derived from 1 1 1 reflection for face-centered cubic (fcc) crystal of metallic Au was identified at $2\theta_B$ = 38.3° (marked with ▼ in Fig. 1).

For all the samples, the major peaks were originated from LDH structure while the peaks due to Au did not appear or were negligibly weak for Au/Zn_2Al-Rec-1, Au/Zn_2Al-Imp-$NaBH_4$, and Au/Zn_2Al-Imp-Lysine above the detection limit of XRD apparatus used. The XRD results indicated that the samples obtained by impregnation followed by liquid reduction (Au/Zn_2Al-Imp-$NaBH_4$ and Au/Zn_2Al-Imp-Lysine) did not comprise [mixed] metal oxides of Zn and/or Al (Fig. 1e, f).

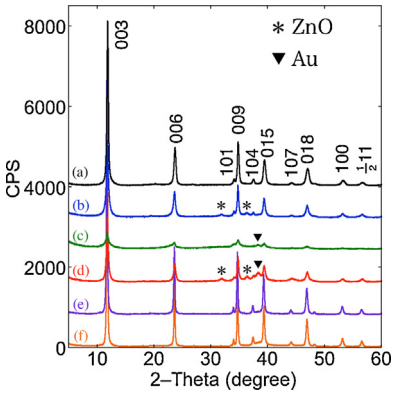

Fig. 1. XRD pattern for Zn_2Al-LDH (a), Au/Zn_2Al-Rec-1 (b), Au/Zn_2Al-Rec-2 (c), Au/Zn_2Al-*Rec*-3-Light (d), Au/Zn_2Al-Imp-$NaBH_4$ (e), and Au/Zn_2Al-Imp-Lysine (f).

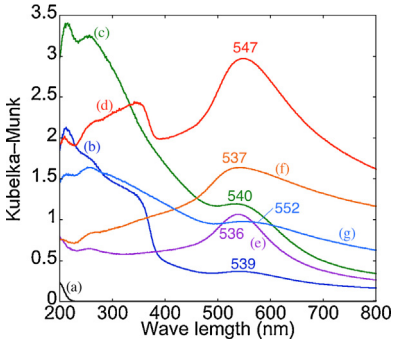

Fig. 2. UV–vis absorption spectrum of Zn_2Al-LDH (a), Au/Zn_2Al-Rec-1 (b), Au/Zn_2Al-Rec-2 (c), Au/Zn_2Al-*Rec*-3-Light (d), Au/Zn_2Al-Imp-$NaBH_4$ (e), Au/Zn_2Al-Imp-Lysine (f), and Au/Zn_2Al-Light (g).

3.2. UV–visible spectra

UV–visible absorption spectra for the Au-LDHs photocatalysts are depicted in Fig. 2. In the spectra for Au/Zn_2Al-Rec-1, Au/Zn_2Al-Rec-2, and Au/Zn_2Al-*Rec*-3-Light, a peak appeared due to SPR of AuNPs at 539 nm, 540 nm, and 547 nm, respectively (Fig. 2b–d). SPR peaks centered at 533–553 nm were previously reported for 2.9–3.4 nm size of AuNPs embedded on LDH [16]. The red shift of the SPR peak from 539 nm (for Au/Zn_2Al-Rec-1) to 547 nm (for Au/Zn_2Al-*Rec*-3-Light) suggested the quantum size effect of AuNPs leading to lower-energy plasmonic near-field when AuNPs grew during LDH reconstruction under UV–visible light irradiation.

The band gap values for support materials were evaluated based on Davis–Mott equation (Table 1). The band-gap values for Zn_2Al-LDH (5.7 eV; Table 1a) apparently decreased to 3.1–2.5 eV for AuNP–LDHs via the reconstruction route (Table 1b–d). It was not due to the change of electronic property of LDH support but can be ascribed to the presence of minor metal oxide phase, e.g. ZnO and/or $ZnAl_2O_4$ and/or the synergetic effects of AuNPs with ZnO/$ZnAl_2O_4$/Zn_2Al-LDH. In the UV–visible spectra of Au/Zn_2Al-Imp-$NaBH_4$ and Au/Zn_2Al-Imp-Lysine (Fig. 2e, f), the characteristic absorption edge at ~400 nm did not appear. This absorption edge is due to ZnO and/or spinel metal oxides: $ZnAl_2O_4$. Thus, both the XRD and UV–vis absorption results suggested the jointed phases of major LDHs and minor mixed oxides for AuNPs–LDHs composites

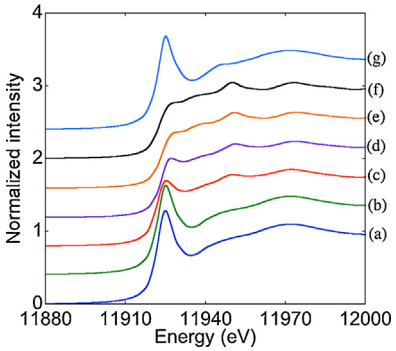

Fig. 3. Normalized Au L_3-edge XANES spectra for Au/Zn_2Al-Rec-1 (a), Au/Zn_2Al-Rec-2 (b), Au/Zn_2Al-*Rec*-3-Light (c), Au/Zn_2Al-Imp-$NaBH_4$ (d), Au/Zn_2Al-Imp-Lysine (e), Au metal foil (f), and Au_2O_3 (g).

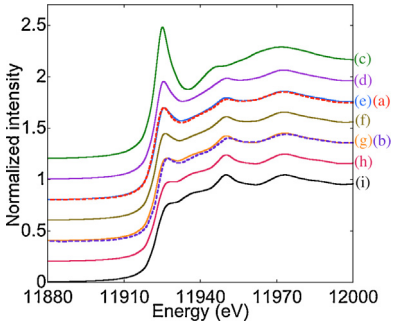

Fig. 4. Comparison of the Au L_3-edge XANES spectra for Au/Zn_2Al-*Rec*-3-Light (a) and Au/Zn_2Al-Imp-$NaBH_4$ (b) to the combination of standard spectra of Au metal foil (Au^{00}) and Au_2O_3 (Au^{3+}). The mixing ratio of Au^{00}:Au^{3+} was progressively varied: 0:100 (c), 55:45 (d), 65:35 (e), 75:25 (f), 85:15 (g), 95:5 (h), and 100:0 (i).

obtained by the LDH reconstruction method. The special environment provided by the transformation of the mixed oxides (ZnO and/or $ZnAl_2O_4$) into the layered LDH structure might give rise to specific photo-responsive properties for the AuNPs–LDHs composites. For Au/Zn_2Al-Imp-$NaBH_4$ and Au/Zn_2Al-Imp-Lysine, the SPR peak due to Au was located at 536 nm and 537 nm, respectively (Fig. 2e, f). The UV–visible spectrum for Au/Zn_2Al-Light was rather featureless and a weak, broad SPR peak appeared at 552 nm.

As will be described based on Au L_3-edge XANES (*see section 3.3*), Au–LDHs comprising Au^0 sites (Au/Zn_2Al-*Rec*-3-Light, Au/Zn_2Al-Imp-$NaBH_4$, and Au/Zn_2Al-Imp-Lysine) exhibited relatively intense SPR peaks (Fig. 2d–f) in clear contrast to weaker SPR peaks for the composites comprising exclusive Au^{3+} sites (Au/Zn_2Al-Rec-1 and Au/Zn_2Al-Rec-2; Fig. 2b, c).

3.3. *Au L_3-edge XANES*

Au L_3-edge XANES spectra measured for Au–LDH composites are depicted in Fig. 3. The spectrum patterns for both Au/Zn_2Al-Rec-1 and Au/Zn_2Al-Rec-2 (spectra a, b) were quite similar to that of Au_2O_3 (spectrum g) while the spectrum e for Au/Zn_2Al-Imp-Lysine was similar to that of Au metal foil (spectrum f). On the other hand, the post-edge pattern for Au/Zn_2Al-*Rec*-3-Light and Au/Zn_2Al-Imp-$NaBH_4$ (spectra c and d) was that between that of Au^{00} and Au^{3+}, demonstrating that the Au sites in these two catalysts were the mixture of Au^0 and Au^{3+}. The spectra for Au/Zn_2Al-*Rec*-3-Light and Au/Zn_2Al-Imp-$NaBH_4$ were fitted with the standard spectra f and g of Au metal (Au^0) and Au_2O_3 (Au^{3+}) by progressively changing the mixing ratio of the two spectra (Fig. 4). The spectra of Fig. 3c and d most resembled mixed spectra with the mixing ratio of Au^0:Au^{3+} = 65:35 (Fig. 3e) and 85:15 (Fig. 3 g), respectively.

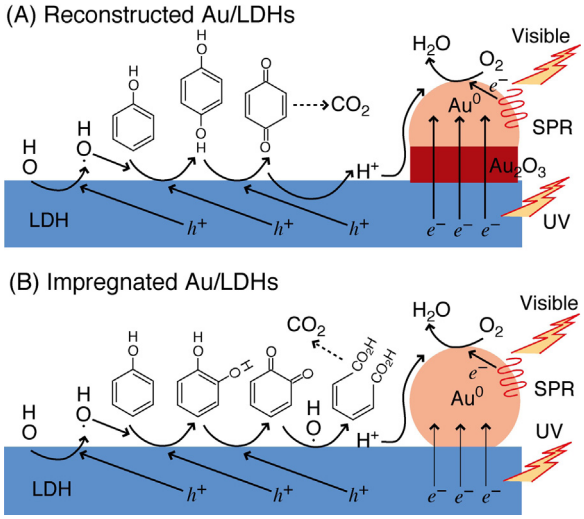

Scheme 1. Proposed reaction mechanism of photocatalytic phenol decomposition on gold species formed on LDH via reconstruction (A) or impregnation (B). Indirect path via *p*-benzoquinone also took place for B, but the rates were lower than those for A. The reaction paths from o-benzoquinone or muconic acid to CO_2 are unknown.

The Au sites were reduced to Au^0 in Au/Zn_2Al-Imp-$NaBH_4$ and Au/Zn_2Al-Imp-Lysine by the effects of $NaBH_4$ and/or lysine. On the other hand, the formation of Au^0 in Au/Zn_2Al-*Rec*-3-Light was the consequence of the electron transfer from Zn_2Al LDH to AuNPs resulted from the charge separation occurred under the irradiation of UV–visible light. Previous results showed that the charge transfer between TiO_2 and the supported AuNPs [38] and between ZnO and the supported Cu ions [28] should suppress the charge recombination thus to maximize its photocatalytic response at surface. Based on these results, the specific charge transfer processes between AuNP and Zn_2Al-LDH in the Au/Zn_2Al-*Rec*-3-Light sample might improve the photocatalytic efficiency.

3.4. *TEM*

Fig. 5 shows representative TEM images and the particle size distribution for AuNPs. Table 1 listed the mean diameter values. TEM images indicated that almost spherical NPs were densely distributed on the Zn_2Al-LDH surface. The mean sizes of the AuNPs were 4.7 nm and 4.9 nm for Au/Zn_2Al-Rec-1 and Au/Zn_2Al-Rec-2, respectively, while mean size for AuNPs increased to 8.5 nm for Au/Zn_2Al-*Rec*-3-Light (Fig. 5a–c and Table 1b–d). Furthermore, together with XANES and TEM results, it was suggested that particle size distribution of AuNPs consisted of Au^{3+} for Au/Zn_2Al-*Rec*-3-Light negligibly change from that of Au/Zn_2Al-Rec-1 while under solar irradiation greater AuNPs consisted of Au^0 than ~5 nm were formed. Thus, particle size distribution for the AuNPs comprising mixed valences of Au^{00} & Au^{3+} in Au/Zn_2Al-*Rec*-3-Light became wider (Fig. 5c). This result reveals an intimate interaction of Au^{3+}NPs with the Zn_2Al-LDH surface during the restoration of the LDH in which Au^{3+}NPs supported on Zn_2Al-LDH would be able to accept electrons quite effectively from the LDH surface to form Au^{00}NPs (Scheme 1A). To obtain more detailed information about the interactions between AuNPs and LDH surface, Au L_3-edge EXAFS was employed to monitor the local structure for Au (see Section 3.5).

For AuNP–LDHs composites obtained by impregnation method the mean diameter of self-supported AuNPs were 4.1 nm for Au/Zn_2Al-Imp-$NaBH_4$ and 7.3 nm for Au/Zn_2Al-Imp-Lysine (Fig. 5d, e and Table 1e, f).

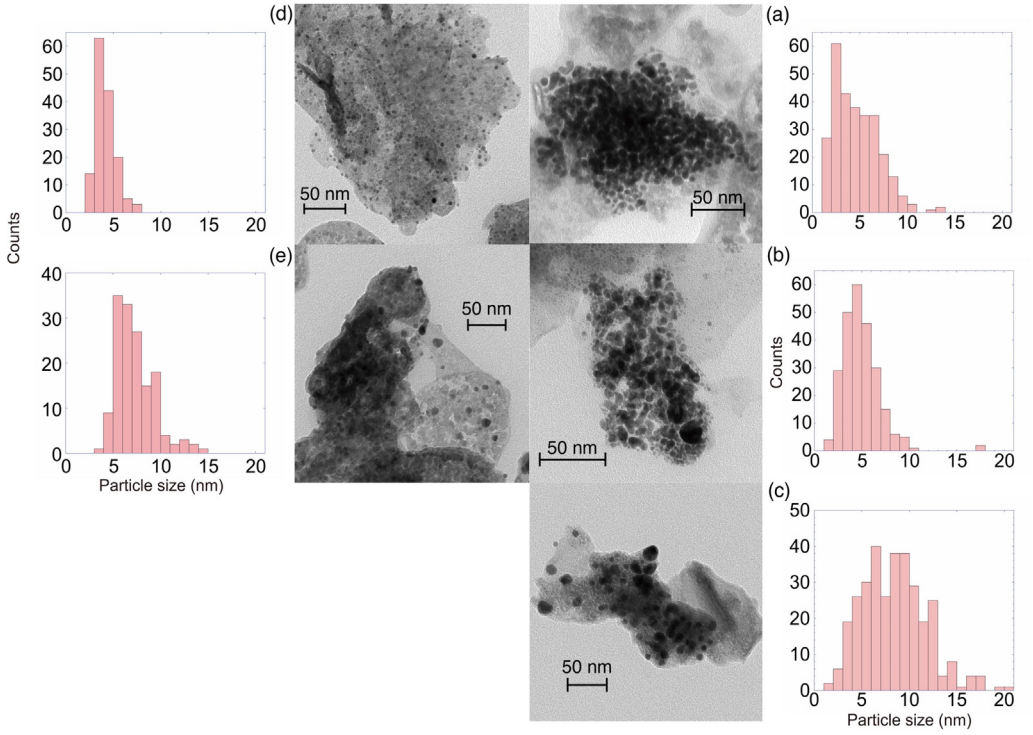

Fig. 5. TEM images and analysis for Au/Zn_2Al-Rec-1 (a), Au/Zn_2Al-Rec-2 (b), Au/Zn_2Al-*R*ec-3-Light (c), Au/Zn_2Al-Imp-$NaBH_4$ (d), and Au/Zn_2Al-Imp-Lysine (e).

3.5. *Au L_3-edge EXAFS*

The coordination environment of AuNPs in AuNP–Zn_2Al-LDH was investigated based on the Au-L_3 edge EXAFS. The k^3-weighted EXAFS function was depicted in Fig. 6. The peaks at 0.16 nm and 0.28 nm (phase shift uncorrected) in the Fourier transform were curve-fit with the parameters of Au–O and Au–Au interatomic pairs, respectively (Fig. 6b, d).

The best-fit results were listed in Table 2. The *N* value of Au–O for Au/Zn_2Al-*R*ec-3-Light was 1.6 and that for Au–Au was 9.0 (Fig. 6-3 and Table 2c), significantly smaller than *N* values for models of Au_2O_3 (4; Table 2f) and Au metal (12; Table 2 g). Namely, the *N* value of Au–O for Au/Zn_2Al-*R*ec-3-Light was 38–43% of *N* value for model Au_2O_3 crystallines taking the fit error values into account. Similarly, the *N* value for Au–Au in Au/Zn_2Al-*R*ec-3-Light was 65–85% of that for Au metal foil taking the fit error values into account.

On the other hand, the *N* values of Au–O for Au/Zn_2Al-Rec-1 and Au/Zn_2Al-Rec-2 samples (both 3.7, Table 2a, b) was much closer to that of Au–O in Au_2O_3. These results demonstrated that the fabrication of the catalyst under irradiation from solar simulator decreased the *N* values of both Au–Au and Au–O shells. Previous studies reported that the decreased *N*(Au–Au) values in AuNPs–LDHs composites indicate stronger interactions between the nanosized Au and LDHs surface [20]. Thus, Zn_2Al-LDH reconstruction in the aqueous solution of Au acetate under the irradiation of UV–visible light should give rise to closer interactions between Zn_2Al-LDH and the supported Au nanoparticles.

The mean particle size for Au suggested by *N*(Au–Au) value for Au/Zn_2Al-*R*ec-3-Light (9.0; Table 2c), Au/Zn_2Al-Imp-$NaBH_4$ (11.3; Table 2d), and Au/Zn_2Al-Imp-Lysine (11.8; Table 2e) were 2.5 nm, 4.8 nm, and 5.3 nm, respectively, assuming fcc crystalline packing [39]. These values were significantly smaller than those obtained using TEM images (8.5 nm, 4.1 nm, and 7.3 nm, respectively, Table 1d–f). The reasons of this discrepancy would be that smaller NPs were not observable in TEM and thus TEM tends to overestimate the nanoparticle size and/or that the size of Au oxides was neglected in the estimation based on *N*(Au–Au) values of EXAFS. In fact, the mean values by TEM (7.3 nm) and by EXAFS (5.3 nm) were relatively close for exclusive Au^{00}NPs in Au/Zn_2Al-Imp-Lysine (Table 1f).

Only Au–Au peak was observed for Au/LDHs obtained by impregnation method (Fig. 6-4, 6-5 and Table 2d, e). Thus, EXAFS results provided further evidence for direct interactions of the surface self-supported AuNPs and Zn_2Al-LDH layers.

3.6. *BET surface area*

The S_{BET} value was 97 $m^2\,g^{-1}$ for Zn_2Al-LDH (Table 1a) in consistent with reported values for LDHs of similar composition (33–83 $m^2\,g^{-1}$) [22,23]. The value decreased by a factor of 0.61–0.84 times for reconstructed LDH samples in the presence of Au (Table 1b–d) or by a factor of 0.56–0.69 times for impregnated Au/LDHs (Table 1e, f). The decrease was not simply correlated to the preparation method of catalysts or Au contents (Table 1).

3.7. *Photocatalytic tests*

Phenol was chosen as a molecule to represent toxic organic compounds with low degradability. The suitability of AuNPs–Zn_2Al-LDHs for photocatalytic decomposition of phenol was evaluated from aqueous solutions under irradiation with simulated solar light. Fig. 7 shows the evolution of the UV–visible absorption profiles for reaction solution during the course of irradiation time. Blank tests without photocatalyst or solar light revealed negligible photocatalytic activities less than 99% degradation of phenol, verifying that phenol degradation reaction was driven via photocatalytic process.

For all the AuNPs–Zn_2Al-LDH catalysts, the characteristic absorbance at 270 nm for phenol decreased as the photo-reaction time elapsed. Unsupported Zn_2Al-LDH exhibited only 7.6% of decrease at 5 h of irradiation from the phenol absorbance at 0 min (Fig. 7a), demonstrating that only LDH was insufficient for degrad-

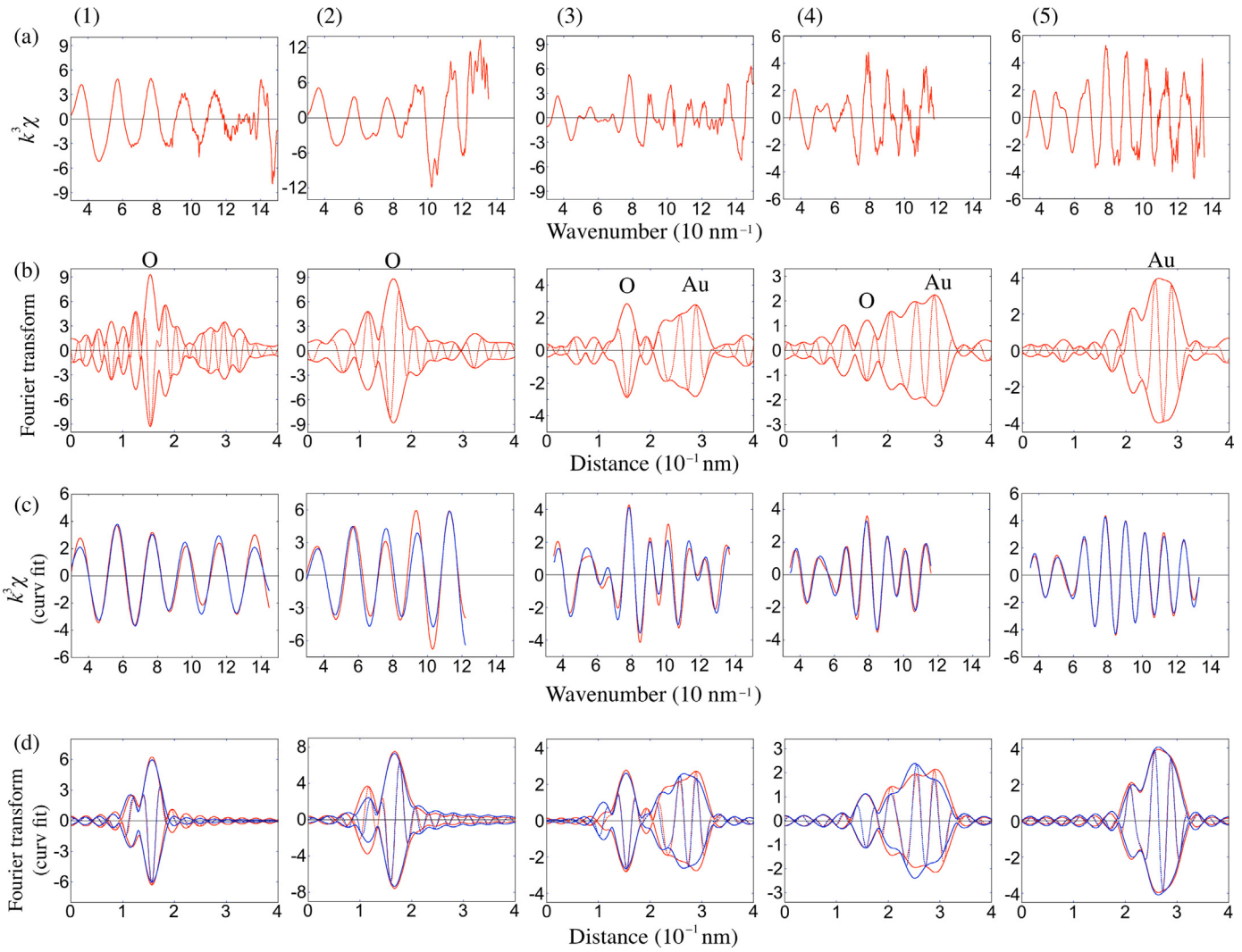

Fig. 6. Au L_3-edge EXAFS for Au/Zn_2Al-Rec-1 (1), Au/Zn_2Al-Rec-2 (2), Au/Zn_2Al-*Rec*-3-Light (3), Au/Zn_2Al-Imp-$NaBH_4$ (4), and Au/Zn_2Al-Imp-Lysine (5). k^3-weighted EXAFS χ oscillation (a), its associated Fourier transform (b), and best-fit results in *k*-space (c) and *R*-space (d). The red (or thin) line represents the experimental values, and the blue (or thick) line represents calculated values in panels b and d. The solid line represents the magnitude and the dotted line represents the imaginary part in panels c and d. (For interpretation of the references to colour in this figure legend, the reader is referred to the web version of this article.)

ing phenol under solar light. This fact indicates the essential contribution of AuNPs to the photocatalytic process.

It was established that phenol photodecomposition could follow different pathways following either a direct oxidative opening process of the aromatic ring, in which muconic acid is formed from o-benzoquinone, or an indirect ring cleavage process to hydroxylated phenolic intermediates e.g. *p*-benzoquinone/hydroquinone as primary intermediate species [36,39]. The peaks at 246, 263, 270, 275, and 289 nm were reported to appear in the UV absorption region for *p*-benzoquinone, trans,trans-muconic acid, phenol, catechol, and hydroquinone [36,40] and in fact confirmed for 4.3–74 ppm of standard aqueous solutions (Fig. 7h). In this regard, differences were observed between the Au–LDH composite catalysts obtained by reconstruction and impregnation methods. Namely, for Au/Zn_2Al-Rec-1, Au/Zn_2Al-Rec-2 and Au/Zn_2Al-*Rec*-3-Light (Fig. 7b–d), formation of *p*-benzoquinone, identified as a characteristic absorption at 248 nm, showed that phenol degradation underwent through hydroxylated phenolic intermediates (Fig. 8B) *versus* both indirect and direct opening process of aromatic using Zn_2Al-LDH and impregnated Au photocatalysts on LDH (Fig. 7a, e–g). The peak intensity was evaluated based on peak deconvolution using equation 3 as a function of wavelength. Quantum mechanically, it would be strict to deconvolute peaks as a function of wave number, i.e. the dimension of energy. The time course in Fig. 7d was replotted as a function of wave number (Fig. S1). It looks almost identical to Fig. 7d except for the direction of horizontal axis is inverse and we believe that the fit using equation 3 as a function of wavelength makes sense.

For reconstructed Au–LDHs, the peak intensity at 248 nm reached a maximum at 40–60 min from the start of irradiation (Fig. 8B-b–d), however, corresponding peak due to hydroquinone at 288 nm was not detected during the time course probably due to the quick oxidative conversion to thermodynamically more stable *p*-benzoquinone. Among them, Au/Zn_2Al-*Rec*-3-Light was the most active based on the decrease of phenol absorbance at 270 nm (Fig. 8A-d). Interestingly, for Au/Zn_2Al-Rec-2, the peak intensity of *p*-benzoquinone decreased for initial 4 h but instead slightly increased after 5 h of irradiation (Fig. 8B-c). It appears that most likely cause was the balance of the rates of phenol photooxidation and the redox equilibrium between hydroquinone and *p*-benzoquinone:

$$HO(surface) + h^+ \rightarrow {}^{\bullet}OH \quad (4)$$

$$Phenol + {}^{\bullet}OH + h^+ \rightarrow Hydroquinone + H^+ \quad (5)$$

Table 2
The curve-fit analysis results of Au L_3-edge EXAFS for Au/Zn_2Al LDH samples.

Entry	Sample	Au–O R (nm) *N* $\Delta\sigma^2$ (10^{-5} nm^2)	Au–Au	Goodness of fit
a	Au/Zn_2Al-Rec-1	0.197 (±0.001) 3.7 (±0.9) 0.8 (±0.1)		4.1×10^3
b	Au/Zn_2Al-Rec-2	0.204 (±0.002) 3.7 (±0.3) 0.3 (±0.1)		1.0×10^3
c	Au/Zn_2Al-Rec-3-Light	0.195 (±0.002) 1.6 (±0.1) 0.1 (±0.4)	0.2888 (±0.0004) 9.0 (±1.2) 0.3 (±0.1)	8.2×10^2
d	Au/Zn_2Al-Imp-$NaBH_4$	0.199 (±0.005) 0.3 (±0.2) 0.1 (±0.5)	0.287 (±0.001) 11.3 (±0.6) 0 (±0.1)	2.8×10^2
e	Au/Zn_2Al-Imp-Lysine		0.287 (±0.001) 11.8 (±0.7) 0.18 (±0.04)	1.0×10^2
Models				
f	Au_2O_3	0.2013 4 –		–
g	Au metal		0.2884 12 –	–

$$\text{Hydroquinone} + 2\,h^+ \rightarrow \text{p-Benzoquinone} + 2H^+ \quad (6)$$

$$p\text{-Benzoquinone} + 6O_2 \rightarrow \ldots \rightarrow 6CO_2 + 2H_2O. \quad (7)$$

For Au/Zn_2Al-Imp-$NaBH_4$ and Au/Zn_2Al-Imp-Lysine, we clearly observed the increase in the broadness of the absorption around 270 nm. This suggests the formation of muconic acid (260 nm) and catechol (276 nm) in addition to phenol (270 nm) in the reaction solution. Thus in the proposed reaction path for the second group, in addition to initial indirect ring opening via *p*-benzoquinone based on the 248-nm peak maximum at 20–40 min from the start of irradiation (Fig. 8B-a, e–g), the oxidation of catechol to o-benzoquinone and the direct opening of the aromatic ring of o-benzoquinone to muconic acid also occurred [36]:

$$\text{Phenol} + \cdot OH + h^+ \rightarrow \text{Catechol} + H^+ \quad (8)$$

$$\text{Catechol} + 2\,h^+ \rightarrow \text{o-Benzoquinone} + 2H^+ \quad (9)$$

$$o\text{-Benzoquinone} + 2{\cdot}OH \rightarrow \text{muconicacid} \quad (10)$$

$$\text{muconicacid} + 11/2O_2 \rightarrow \ldots \rightarrow 6CO_2 + 3H_2O. \quad (11)$$

Thus, different reaction paths were revealed between these two types of catalysts. Fig. 8 shows the results for measured absorbance of each deconvoluted peak using Gaussian functions. The activity sequence of the catalysts after 160 min of irradiation under UV–visible light was in the order (phenol degradation ratio in the parenthesis):

$$\text{Au/Zn}_2\text{Al-}Rec\text{-3-Light(100\%)} > \text{Au/Zn}_2\text{Al-Rec-1(70.1\%)} > \text{Au/Zn}_2\text{Al-Light(52.3\%)} > \text{Au/Zn}_2\text{Al-Rec-2(25.4\%)} \sim \text{Au/Zn}_2\text{Al-Imp-NaBH}_4\text{(26.0\%)} \sim \text{Au/Zn}_2\text{Al-Imp-Lysine(22.5\%)} > \text{Zn}_2\text{Al-LDH(17.6\%)}. \quad (12)$$

Au/Zn_2Al-*Rec*-3-Light was the most active in degrading phenol under simulated solar irradiation. The major reaction routes via equations 4–7 based on the monitoring using UV–visible spectroscopy should be confident with the confirmation of peaks of phenol and *p*-benzoquinone by HPLC equipped with a column Shim-pack VP-ODS using the mixed solution of acetonitrile and 10 mM sodium phosphate buffer as a carrier. However, the calibration of the amount only for *p*-benzoquinone was difficult in the standard mixed solutions of *p*-benzoquinone (0.1–2.0 ppm), trans,trans-muconic acid (0.1–2.0 ppm), phenol (5.0–100 ppm), catechol (5.0–100 ppm), and hydroquinone (5.0–100 ppm) presumably due to the equilibrium between *p*-benzoquinone and hydroquinone (equation 6). The calibration of hydroquinone using HPLC was confident due to the difference of sensitivity (molar absorption coefficient) between *p*-benzoquinone and hydroquinone (Fig. 7h). This equilibrium may be also related to the fact that no hydroquinone peak was observed in the photo-decompsition monitoring using UV–visible spectroscopy (Fig. 7a–g). Improved HPLC analyses will be published elsewhere [41].

Furthermore, photodecomposition of acetophenone (25 mg L^{-1}) was also monitored to check the availability of UV–visible monitoring for the other catalytic reaction (Supplementary data). The reactivity order was

$$\text{Au/Zn}_2\text{Al-}Rec\text{-3-Light} > \text{Au/Zn}_2\text{Al-Rec–1} > \text{Au/Zn}_2\text{Al-Light} > \text{Au/Zn}_2\text{Al-Imp-NaBH}_4, \quad (13)$$

similar as in equation 12.

Au/Zn_2Al-Rec-1 showed slightly less catalytic activity with 70% phenol degradation ratio of that using Au/Zn_2Al-Rec-3-Light for 160 min of reaction. Note that Au/Zn_2Al-Rec-3-Light, Au/Zn_2Al-Rec-1, and Au/Zn_2Al-Light have essentially identical chemical compositions in LDH and also Au content although chemical states were different in AuNPs: a mix state of Au^0 and Au^{3+} in Au/Zn_2Al-Rec-3-Light *versus* exclusive Au^{3+} in Au/Zn_2Al-Rec-1. Hence, balancing the oxidation state of AuNPs should clearly influence the photocatalytic performance.

Increasing Au content in Au/Zn_2Al-Rec-2 steadily declined the phenol degradation ratio to 25% for 160 min of reaction (Fig. 8A-c) and p-benzoquinone was accumulated (Fig. 8B-c). Furthermore, Au–Zn_2Al catalysts obtained by impregnation-reduction method showed slightly less photocatalytic activity, with 26–23% phenol degradation over the same time frame. For quantitative comparison between the catalysts, specific rates (μmol L^{-1} h^{-1}) were calculated based on the derivative of phenol amount as a function of time

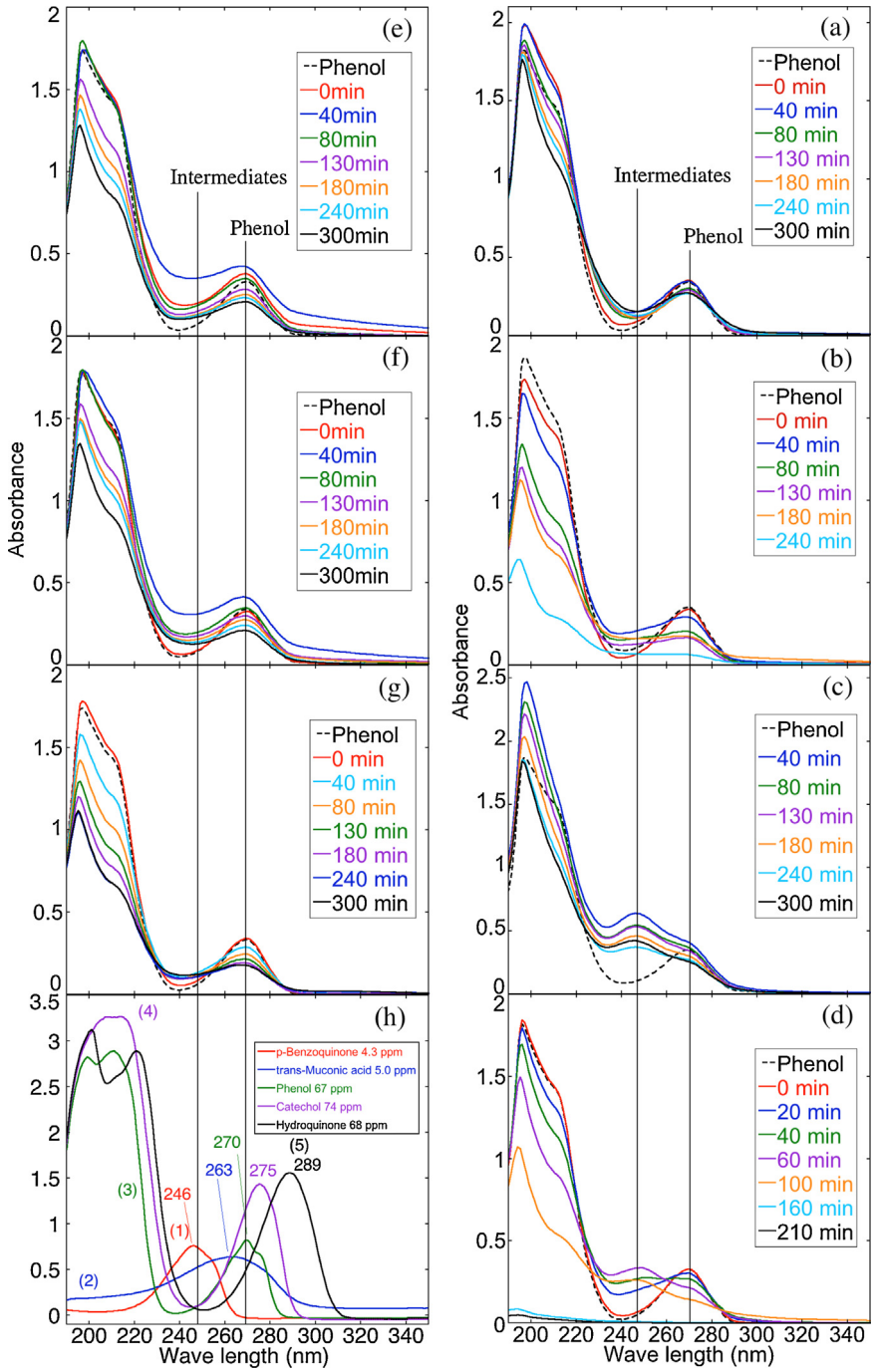

Fig. 7. UV–vis absorption spectrum of phenol photo degradation time course for Zn_2Al-LDH (a), Au/Zn_2Al-Rec-1 (b), Au/Zn_2Al-Rec-2 (c), Au/Zn_2Al-Rec-3-Light (d), Au/Zn_2Al-Imp-$NaBH_4$ (e), Au/Zn_2Al-Imp-Lysine (f), Au/Zn_2Al-Light (g), *p*-benzoquinone (4.3 ppm; h1), trans,trans-muconic acid (5.0 ppm; h2), phenol (67 ppm; h3), catechol (74 ppm; h4), and hydroquinone (68 ppm; h5).

(Table 1):

$$\text{Au/Zn}_2\text{Al-Rec-3-Light}(199) > \text{Au/Zn}_2\text{Al-Rec-1}(125) > \text{Au/Zn}_2\text{Al-Light}(68) > \text{Au/Zn}_2\text{Al-Rec-2}(47) \sim \text{Au/Zn}_2\text{Al-Imp-NaBH}_4(42) \sim \text{Au/Zn}_2\text{Al-Imp-Lysine}(43) > \text{Zn}_2\text{Al-LDH}(25). \quad (14)$$

It was also apparent from the rates that Au/Zn_2Al-Rec-3-Light showed a maximum rate for phenol degradation and the order of the rates was essentially identical to the order of degradation extent in equation 12. The results showed that Au^0-based catalysts were approximately four orders of magnitude less active than Au/Zn_2Al-Rec-3-Light comprising a mixed valence state of Au^0/Au^{3+}.

In fact, the numbers of surface-exposed Au^0 sites were estimated for Au/Zn_2Al-Rec-3-Light, Au/Zn_2Al-Imp-$NaBH_4$, and Au/Zn_2Al-Imp-Lysine based on mean Au particle size by TEM and cubo-octahedron model [42] (Table 1d–f). The values 27 $\mu mol\ g_{cat}^{-1}$, 31 $\mu mol\ g_{cat}^{-1}$, and 19 $\mu mol\ g_{cat}^{-1}$, respectively, show no correlation to photocatalytic rates of phenol decomposition. Furthermore, BET surface area was evaluated for catalysts after phenol photodecomposition tests for 5 h (Table 1). The activity order is written again with the BET surface area in the parenthesis:

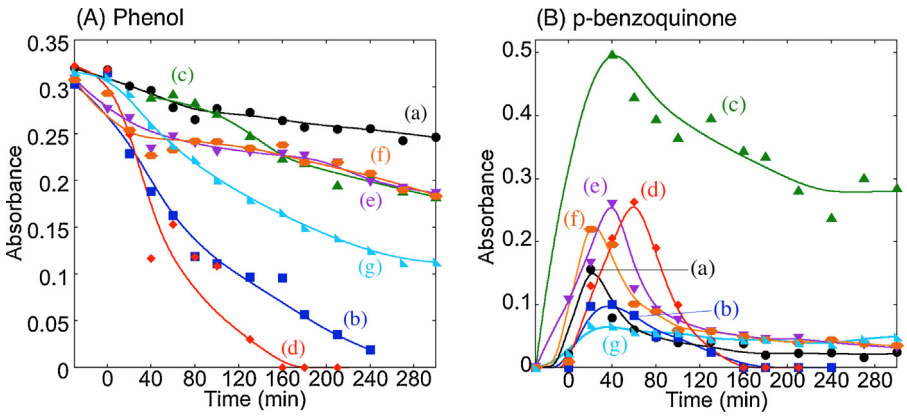

Fig. 8. The time course for peak at 270 nm (phenol; A) and at 248 nm (*p*-benzoquinone; B) evaluated based on Gaussian deconvolution during phenol photo-degradation for Zn_2Al-LDH (a), Au/Zn_2Al-Rec-1 (b), Au/ZnAl-Rec-2 (c), Au/Zn_2Al-*R*ec-3-Light (d), Au/Zn_2Al-Imp-$NaBH_4$ (e), Au/Zn_2Al-Imp-Lysine (f), and Au/Zn_2Al-Light (g).

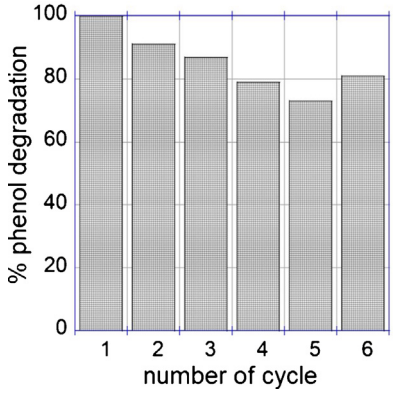

Fig. 9. The photocatalytic activity for six cycles of phenol decomposition. Before the 6th cycle, the catalyst was kept during 1 h under solar irradiation using Au/Zn_2Al-*R*ec-3-Light.

$$\text{Au/Zn}_2\text{Al-Rec-3-Light}(79\,\text{m}^2\,\text{g}^{-1}) > \text{Au/Zn}_2\text{Al-Rec-1}(81\,\text{m}^2\,\text{g}^{-1}) > \text{Au/Zn}_2\text{Al-Rec-2}(59\,\text{m}^2\,\text{g}^{-1}) \sim \text{Au/Zn}_2\text{Al-Imp-NaBH}_4(54\,\text{m}^2\,\text{g}^{-1}) \sim \text{Au/Zn}_2\text{Al-Imp-Lysine}(67\,\text{m}^2\,\text{g}^{-1}) > \text{Zn}_2\text{Al-LDH}(97\,\text{m}^2\,\text{g}^{-1}). \quad (14')$$

It was difficult to find the correlation between the BET surface area and he photocatalytic activity order. Thus, Au^0 sites and specific surface area were directly not related to photocatalytic activity.

We also noticed that Au/Zn_2Al-Rec-3-Light showed the highest intensity for the SPR response of AuNPs (see Fig. 2d), although a systematic correlation between the SPR intensity of the self-supported AuNPs and the photocatalytic efficiency of the studied catalysts was not found mostly due to the difference of SPR response between Au^0 and Au^{3+} sites. Furthermore, as shown in Table 1b, c, and e, there was no remarkable difference in AuNPs mean particles sizes of Au/Zn_2Al-Rec-1, Au/ZnAl-Rec-2, and Au/Zn_2Al-Imp-$NaBH_4$ (4.1–4.9 nm) based on TEM images. On the other hand, a slight variation was observed for Au/Zn_2Al-Rec-3-Light and Au/Zn_2Al-Imp-Lysine with a mean size of AuNPs of 8.5 and 7.3 nm, respectively (Table 1d, f). Thus, small extent of increase of AuNPs mean size affected no impact on the photocatalytic activity.

In view of its application, the stability of the photocatalyst is also important and needs to be evaluated. The best Au/Zn_2Al-Rec-3-Light photocatalyst was tested for the reusability. Fig. 9 shows the recycling experiments of Au/Zn_2Al-Rec-3-Light for phenol degradation under solar irradiation. The degradation rates using photocatalysts were 100%, 91.2%, 86.8%, 78.9%, and 72.8% in the first, second, third, fourth, and fifth cycle of tests (160 min-irradiation for each cycle). The catalyst efficiency still remained at 73% of initial activity after the fifth successive recycle tests. Furthermore, the used Au/Zn_2Al-Rec-3-Light sample was separated from the reactor after the fifth cycle and irradiated for 1 h under UV–visible light. After the light treatment, the catalyst was tested again for phenol photo-decomposition. Confidently, the efficiency for phenol degradation increased to 80.9% of initial activity, increased from 72.8% in the fifth cycle. This behavior might be relied on the particular charge transfers in the intimately mixed phases of AuNPs and Zn_2Al-LDHs evolved under the irradiation with UV–visible light.

AuNPs leaching, a possible explanation for the decrease in efficiency was independently ruled out by centrifuging the reaction mixture after each cycle. No further reaction of phenol was observed when the supernatant was mixed with the fresh phenol solution under the solar irradiation, demonstrating a minimal/no contribution from leached AuNPs. Furthermore, the UV–visible analysis of the supernatant did not detect SPR effect of AuNPs pointing out that nano-sized gold species was not present in the supernatant. The leaching of Zn or Al from the LDH layers might occur only at acidic pH (lower than 3) while the pH of the phenol aqueous solutions used during the experiments (containing also the catalyst) was around 7.5.

4. Discussion

4.1. Electronic and structure characteristics of AuNPs on AuNPs/LDHs interface

Photocatalytic phenol decomposition rates followed the order of equation 12. Basically, photocatalysts comprising Au embedded during the reconstruction of LDH layers were superior to impregnated Au on LDH using chemical reductant and/or surfactant or unsupported LDH (Fig. 8). Typical difference between these two groups was the valence state of Au atoms in AuNPs: major valence state was Au^{3+} in the former AuNP–LDHs via reconstruction route *versus* major metallic Au^0 state in the latter Au photocatalysts impregnated on LDH based on Au L_3-edge XANES.

In the photocatalytic activity order of phenol decomposition in equation 12, Au/Zn_2Al-Rec-3-Light was especially active and 30 mg L^{-1} of phenol was completely decomposed to lower than detection limit within 160 min of UV–visible light irradiation (Figs. 7d and 8d). The valence state of Au was evaluated to Au^0:Au^{3+} of 65: 35 based on the comparison to the mixture of Au L_3-

edge XANES spectra for Au metal and Au_2O_3 by changing the mixing ratio of the two (Fig. 4a, e).

The coordination of Au sites in Au/Zn_2Al-Rec-3-Light was further investigated by Au L_3-edge EXAFS analyses (Fig. 6-3). Both Au–Au and Au–O peaks in the Fourier transform were clearly observed only for this sample among the AuNP–LDH samples via reconstruction. In fact, both Au–O peak with the *N* value of 1.6 (4 for Au_2O_3 crystallites) and Au–Au peak with the *N* value of 9.0 (12 for Au metal) were given based on the curve-fit analysis (Table 2c). These reduced *N* values compared to bulk crystallites/crystals suggested mean 8.5 nm of AuNPs embedded on LDH surface (TEM, Fig. 5c). The reconstruction of LDH was taking place in a complex environment in which the mixture of ZnO and $ZnAl_2O_4$ was able to reconstruct the brucite-like Zn_2Al-LDH layers. Such a specific environment might facilitate particular phases junctions between ZnO/$ZnAl_2O_4$/Zn_2Al-LDH and the evolved AuNPs where Au^{3+} ions should bind with their surface to constitute thin Au_2O_3 interface phase and diffused electrons originating from the charge separation by UV–visible light irradiation during the reconstruction process should reduce surface Au sites to Au^0 (Scheme 1A). The interface of Au_2O_3 phase between metallic Au^0 and LDH might facilitate the electron transfer from semiconducting LDH to Au sites for O_2 reduction during aerobic phenol photo-decomposition whereas the metallic Au^0NPs were not effectively embedded on the LDH surface for impregnated AuNP–LDH samples thereby the electron transfer at the interface was slower and the charge separation efficiency was lower.

Furthermore, the comparison of Debye–Waller factors ($\Delta\sigma^2$) obtained in EXAFS analysis revealed that Au^0 had a higher disorder in Au/Zn_2Al-Rec-3-Light ($\Delta\sigma^2$ Au–Au: 0.3×10^{-5} nm^2) than in the AuNP–LDHs obtained via impregnation ($\Delta\sigma^2$ Au–Au: 0×10^{-5} nm^2 and 0.18×10^{-5} nm^2) due to specific interaction between AuNP and LDH during reconstruction [43] while the Au–O showed the lowest disorder in Au/Zn_2Al-Rec-3-Light ($\Delta\sigma^2$ 0.1×10^{-5} nm^2) compared to other reconstructed AuNP–LDHs ($\Delta\sigma^2$ 0.3×10^{-5}–0.8×10^{-5} nm^2) comprising dominant Au^{III} sites probably due to the difference between the Au oxide interface sites and Au oxide NP sites.

4.2. Proposed reaction mechanism of phenol photodecomposition utilizing various states of Au on LDH

The other difference between the first group, AuNP–LDHs via reconstruction, and the second group, obtained by impregnation of Au on LDH, was the photocatalytic reaction pathway: via indirect ring cleavage mechanism to p-benzoquinone and/or other hydroxylated phenolic intermediates *versus* both indirect and direct oxidative ring opening processes, respectively. Thermodynamically more stable p-benzoquinone compared to hydroquinone would be formed via reaction of phenol with a hole and hydroxy radical (produced from a hole & surface hydroxy; equation 4) to hydroquinone (equation 5) on LDH surface under the irradiation of UV–visible light followed by further two electron oxidation by holes to p-benzoquinone (equation 6). These oxidation reaction steps would be accelerated by the effective charge transfer at the interface between AuNPs and LDH and the resultant better charge separation efficiency as the assembly. Using anatase-type TiO_2, boron-doped anatase TiO_2, and Au and/or Pd-doped TiO_2 under UV–visible light, a peak at 289 nm due to hydroquinone gradually increased associated with the decrease of peak decrease at 270 nm due to phenol, but any clear peak at 248 nm due to p-benzoquinone was not observed [31,44]. This difference suggested that the photo-oxidation from hydroquinone to p-bezoquinone was favorable over LDH surface (Scheme 1A) *versus* significant photo-reduction from p-benzoquinone to hydroquinone over TiO_2-based photocatalysts. The stabilization of p-benzoquinone was also pointed out for CeO_2–ZnTi-LDH photocatalyst via LDH reconstruction route [36]. However, the photocatalytic contribution of impurity level of metal oxide phases, e.g. ZnO and $ZnAl_2O_4$, detected for the first group, AuNP–LDHs via reconstruction, as detected for active photocatalysts in XRD (Fig. 1b, d) cannot be totally excluded because the charge separation efficiency using metal oxides is in general superior to that using metal hydroxides.

In the second group of photocatalysts, the peak due to p-benzoquinone at 248 nm appeared after 20–40 min suggesting indirect ring opening, however the peak was weaker (Fig. 8B-a, e–g) than that in the first group, especially for Au/Zn_2Al-Rec-2 and Au/Zn_2Al-Rec-3-Light (Fig. 8B-c, d), suggesting that direct ring cleavage mechanism also proceeded. In fact, the minor contribution of muconic acid (260 nm) and catechol (276 nm) was suggested based on the broader peak width centered at 270 nm (phenol), especially for Au/Zn_2Al-Imp-$NaBH_4$ and Au/Zn_2Al-Imp-Lysine during the time course of phenol decomposition irradiated by light (Fig. 7a, e–g). It should be noted that p-benzoquinone was detected after 40–60 min for the first group but that the phenol decomposition rates to CO_2 and H_2O (equation 7) was faster using first group, especially using Au/Zn_2Al-Rec-3-Light: total mineralization at 160 min (Fig. 7d). Thus, the rates from phenol to p-benzoquinone (Scheme 1A) should be significantly accelerated for the first group compared to the rates from phenol to muconic acid (Scheme 1B) due to greater amount of diffused holes owing to the effective charge separation for reconstructed AuNP–LDH assembly.

This study provides experimental evidence that to design efficient AuNPs–LDHs for solar energy photocatalysis the tailored construction for specifically designed the characteristics of the phase junctions between AuNPs and LDH is required.

5. Conclusions

AuNPs formed via reconstruction route of LDH in Au(III) acetate aqueous solution was compared to AuNPs impregnated on LDH and reduced by $NaBH_4$ and/or lysine. The LDH reconstruction was performed in the presence/absence of UV–visible light. AuNPs impregnated in LDH in the presence of UV–visible light were also prepared from comparison. The activity of phenol photo-decomposition was in the order Au/Zn_2Al-Rec-3-Light Au/Zn_2Al-Rec–1 > Au/Zn_2Al-Light > Au/Zn_2Al-Rec–2 ~ Au/Zn_2Al-Imp-$NaBH_4$ ~ Au/Zn_2Al-Imp-Lysine > Zn_2Al-LDH. Thus, AuNPs were essential for the photocatalysis and reconstructed AuNP–LDHs were basically superior to impregnated AuNP–LDHs. Among them, Au/Zn_2Al-Rec-3-Light prepared via LDH reconstruction irradiated by UV–visible light was the best and totally photo-decomposed 50 mg L^{-1} of phenol in 160 min. In the catalyst, approximately 5 nm of Au^0NPs were embedded on LDH surface through Au_2O_3 layers as revealed by Au L_3-edge XANES and EXAFS. Charges (electrons and holes) in the Au–LDH assembly separated by light were effectively diffused to Au^0NPs and LDH surface and reduced O_2 and proceeded indirect ring-opening mechanism to hydroquinone and then to p-benzoquinone, respectively. As the unsupported LDH negligibly photo-decomposed phenol, AuNPs were essential and directly incorporated in the catalysis. AuNPs impregnated on LDH under the UV–visible irradiation (not reconstruction route) or reduced using $NaBH_4$ and/or lysine were less active and decomposed phenol via both indirect mechanism via p-benzoquinone and direct ring-opening mechanism to catechol, o-benzoquinone, and then to muconic acid.

Acknowledgments

The authors are grateful for the financial supports from the Grant-in-Aid for Scientific Research C (26410204, 22550117) from Japan Science Promotion Agency, Japan and from the Romanian National Authority for Scientific Research, CNCS-UEFISCDI (PN-II-ID-PCE-75/2013), Romania. X-ray absorption experiments were conducted under the approval of the Photon Factory Proposal Review Committee (2014G631, 2012G683, 2011G033), Japan. The authors thank Shimadzu Corporation for the HPLC analyses.

Appendix A. Supplementary data

Supplementary data associated with this article can be found, in the online version, at http://dx.doi.org/10.1016/j.apcatb.2016.06.031.

References

[1] A.A. Herzing, C.J. Kiely, A.F. Carley, P. Landon, G.J. Hutchings, Science 321 (2008) 1331–1335.
[2] A. Cho, Science 299 (2003) 1684–1685.
[3] Y. Yoshida, Y. Izumi, Catal. Surv. Asia, in press, DOI: 10.1007/s10563-016-9216-8.
[4] C. Gomes Silva, Y. Bouizi, V. Fornés, H. García, J. Am. Chem. Soc. 131 (2009) 13833–13839.
[5] J. Gong, Chem. Rev. 112 (2012) 2987–3054.
[6] F. Zhang, X. Zhao, C. Feng, B. Li, T. Chen, W. Lu, X. Lei, S. Xu, ACS Catal. 1 (2011) 232–237.
[7] P. Liu, V. Degirmenci, E.J.M. Hensen, J. Catal. 313 (2014) 80–91.
[8] Y. Zhang, X. Cui, F. Shi, Y. Deng, Chem. Rev. 112 (2012) 2467–2505.
[9] D.B. Ingram, S. Linic, J. Am. Chem. Soc. 133 (2011) 5202–5205.
[10] C.G. Silva, M.J. Sampaio, S.A.C. Carabineiro, J.W.L. Oliveira, D.L. Baptista, R. Bacsa, B.F. Machado, P. Serp, J.L. Figueiredo, A.M.T. Silca, J.L. Faria, J. Catal. 316 (2014) 182–190.
[11] A. Corma, H. Garcia, Chem. Soc. Rev. 37 (2008) 2096–2126.
[12] C. Clavero, Nat. Photonics 8 (2014) 95–103.
[13] O. Nicoletti, F. de la Pena, R.W. Leary, D.J. Holland, C. Ducati, P.A. Midgley, Nature 502 (2013) 80–84.
[14] K. Wu, J. Chen, J.R. McBride, T. Lian, Science 349 (2015) 632–635.
[15] J. Prince, F. Tzompantzi, G. Mendoza-Damian, F. Hernández-Beltrán J.S. Valente,. Appl Catal. B 163 (2015) 352–360.
[16] G. Carja, M. Birsanu, K. Okada, H. Garcia, J. Mol. Mater. Chem. A 1 (2013) 9092–9098.
[17] S. Kawamura, M.C. Puscasu, Y. Yoshida, Y. Izumi, G. Carja, Appl. Catal. A 504 (2015) 238–247.
[18] D. Varade, K. Haraguchi, J. Mater. Chem. 22 (2012) 17649–17655.
[19] A.S. Sharma, H. Kaur, D. Shah, RSC Adv. 6 (2016) 28688–28727.
[20] L. Wang, Y. Zhu, J.-G. Wang, F. Liu, J. Huang, X. Meng, J.-M. Basset, Y. Han, F.-S. Xiao, Nat. Commun. 6 (2015) 1–8 (Article number 6957).
[21] X. Zhao, F. Zhang, S. Xu, D.G. Evans, X. Duan, Chem. Mater. 22 (2010) 3933–3942.
[22] N. Ahmed, Y. Shibata, T. Taniguchi, Y. Izumi, J. Catal. 279 (2011) 123–135.
[23] N. Ahmed, M. Morikawa, Y. Izumi, Catal. Today 185 (2012) 263–269.
[24] H. Wei, J. Yu, J. Zheng, H. Su, X. Wang, Inorg. Chim. Acta 427 (2015) 33–44.
[25] Y. Izumi, T. Itoi, S. Peng, K. Oka, Y. Shibata, J. Phys. Chem. C 113 (2009) 6706–6718.
[26] X. Gao, I.E. Wachs, J. Phys. Chem. B 104 (2000) 1261–1268.
[27] F. Wooten, Optical Properties of Solids, Academic Press, New York, USA, 1972 (142 pp).
[28] Y. Yoshida, T. Itoi, Y. Izumi, J. Phys. Chem. C 119 (2015) 21585–21598.
[29] Y. Ogura, S. Okamoto, T. Itoi, Y. Fujishima, Y. Yoshida, Y. Izumi, Chem. Comm. 50 (2014) 3067–3070.
[30] Y. Izumi, D. Obaid, K. Konishi, D. Masih, M. Takagaki, Y. Terada, H. Tanida, T. Uruga, Inorg. Chim. Acta 361 (2008) 1149–1156.
[31] J.A. Bearden, Rev. Mod. Phys. 39 (1967) 78–124.
[32] G. Zschornack, Handbook of X-ray Data, Berlin/Heidelberg, Springer, 2007.
[33] M. Vaarkamp, H. Linders, D. Koningsberger, XDAP version 2.2.7, XAFS Services International, Woudenberg, The Netherlands, 2006.
[34] L. Xiong, L. Zheng, J. Xu, D. Zheng, J. Li, X. Li, J. Sun, Q. Liu, L. Niu, S. Yang, J. Xia, Environ. Chem. Lett. 9 (2011) 251–257.
[35] K. Matsuo, R. Yonehara, K. Gekko, J. Biochem. 135 (2004) 405–411.
[36] E.M. Seftel, M.C. Puscasu, M. Mertens, P. Cool, G. Carja, Appl. Cat. B 150/151 (2014) 157–166.
[37] J.Q. Qiao, N. Yuan, C.J. Tang, J. Yang, J. Zhou, H.Z. Lian, L. Dong, Resear. Chem. Intermed. 38 (2012) 549–558.
[38] V. Subramanian, E.E. Wolf, P.V. Kamat, J. Am. Chem. Soc. 126 (2004) 4943–4950.
[39] B.J. Kip, F.B.M. Duivenvoorden, D.C. Koningsberger, R. Prins, J. Catal. 105 (1987) 26–38.
[40] L. Xiong, L. Zheng, J. Xu, D. Zheng, J. Li, X. Li, J. Sun, Q. Liu, L. Niu, S. Yang, J. Xia, Environ. Chem. Lett. 9 (2011) 251–257.
[41] G. Mikami, F. Grosu, S. Kawamura, Y. Yoshida, G. Carja, Y. Izumi, manuscript in preparation.
[42] F. Humblot, D. Didillon, F. Lepeltier, J.P. Candy, J. Corker, O. Clause, F. Bayard, J.M. Basset, J. Am. Chem. Soc. 120 (1998) 137–146.
[43] F. Behafarid, J. Matos, S. Hong, L. Zhang, T.S. Rahman, B.R. Cuenya, ACS Nano 8 (2014) 6671–6681.
[44] R. Su, R. Tiruvalam, Q. He, N. Dimitratos, L. Kesavan, C. Hammond, J.A. Lopez-Sanchez, R. Bechstein, C.J. Kiely, G.J. Hutchings, F. Besenbacher, ACS Nano 6 (2012) 6284–6292.